Laminar bubbly flow in an open capillary channel in microgravity

Abdelkader Salim [a,b], Catherine Colin [a,*], Aleksander Grah [b], Michael E. Dreyer [b]

[a] Institut de Mécanique des Fluides de Toulouse, Université de Toulouse, Allée du Professeur Camille Soula, 31400 Toulouse, France
[b] Center of Applied Space Technology and Microgravity, University of Bremen, Am Fallturm, 28359 Bremen, Germany

ARTICLE INFO

ABSTRACT

The study of a bubbly laminar two-phase flow in an open capillary channel under microgravity conditions was conducted aboard the sounding rocket, Texus-45. The channel consists of two parallel plates of width b = 25 mm and distance a = 10 mm. The flow along the length l = 80 mm is confined by a free surface on one side and a plate on the opposite side. The bubbles are injected at the nozzle of the capillary channel via six capillary tubes of 100 μm in inner diameter. Different liquid and gas flow rates were tested leading to different liquid free surface shape and bubble size.

The effect of the gas flow rate on the shape of the free surface is analysed from image processing. The local curvature of the free surface can be related to the local wall friction taking into account the entrance effects in the channel. The wall shear stress is found to be increased in two-phase flow by comparison to single-phase flow. The mean bubble velocities averaged over the channel cross section are also measured by image processing. They are directly proportional to the mixture velocity. The bubble size increases along the channel due to coalescence. The bubble size evolution is well predicted by the coalescence model previously developed by the authors.

© 2010 Elsevier Ltd. All rights reserved.

1. Introduction

Open capillary channels are widely used in space applications for liquid transport and thermal control: Propellant Management Devices of satellites, grooves of heat pipes.

The hydrodynamics and the stability of forced flows in open capillary channels were investigated by Rosendahl et al. (2001, 2004), Haake et al. (2006), Rosendahl and Dreyer (2007), Grah et al. (2008). For an internal liquid pressure lower than ambient gas pressure the free liquid surface is bent inwards and concave at any cross section. Due to the wall friction and the flow acceleration, the pressure decreases in the flow direction and the curvature of the free surface increases constricting the flow path. Below a critical flow rate a steady flow is observed and the capillary pressure at the gas–liquid interface balances the pressure difference between the liquid flow and the surrounding constant gas pressure. If the critical flow rate is exceeded the liquid surface collapses at the channel outlet. In fact, the surface curvature becomes so high that gas is ingested in the liquid flow. Then the flow transits from a steady single-phase flow to an unsteady two-phase flow. In the latter case, the gas can be ingested into the fluid loop as bubbles, and may affect the efficiency of the liquid system. Then, it is vital to know how the flow behaviour in

an open capillary channel is affected by the presence of bubbles. As the liquid free surface shape is very sensitive to pressure variations, the open capillary channel is an interesting geometry to investigate some characteristics of laminar bubbly flows in microgravity (wall shear stress, bubble velocity and bubble size evolution). Since hardware design and manufacturing are very expensive, the existing hardware developed for the study of open capillary channel by Rosendahl and Dreyer (2007) has been reused and modified to allow the study of a laminar bubbly flow in microgravity, that has never been studied before: a new design of the channel geometry was proposed and a air supply circuit and small capillary tubes were added to inject bubbles in the capillary channel.

Laminar bubbly flows have been mainly investigated in normal gravity environment, by several researchers (Kashinsky et al., 1993; Rivière and Cartellier, 1999; Song et al., 2001; Tomiyama et al., 2002; Azpitarte and Buscaglia, 2003; Takamasa et al. 2003; Biswas et al., 2005; Lu et al., 2006). These studies showed a strong tendency for the bubbles to collect near the wall for co-current upward flow and in the pipe center for co-current downward flow. In the last configuration, no bubbles were found for a finite distance away from the channel wall (Kashinsky et al., 1993). Thus, the void profile has a peak near the channel wall and in the channel core in upward and downward flows, respectively. The intensity of the peaks depends on the liquid velocity, gas fraction, the mean bubble diameter and the size distribution (Kashinsky et al., 1993; Song

---

* Corresponding author.
  E-mail address: colin@imft.fr (C. Colin).

et al., 2001; Tomiyama et al., 2002). Kashinsky et al. (1993) confirmed experimentally that the distance between the pipe wall and the wall peak depends both on the bubble size and on the liquid velocity. The tendencies are the same as those classically observed in turbulent flow. The lift and the wall forces are shown to control the void fraction profile in a fully developed laminar flow (Tomiyama et al., 2002; Biswas et al., 2005). Based on the void fraction profile, analytical models were developed separating a developed bubbly laminar flow in a homogeneous region in the channel core and a wall layer region (Azpitarte and Buscaglia, 2003; Lu et al., 2006).

The wall shear stress in bubbly laminar flow in normal gravity was found to be higher than in single-phase flow and highly depends on the flow parameters. For a given velocity and void fraction, the wall shear stress increases as the bubbles size decreases (Kashinsky et al., 1993; Rivière et al., 1999). A higher accumulation of bubbles near the wall region deforms the liquid velocity profile locally and, then, produces a high shear stress. Rivière and Cartellier (1999) showed using a two-fluid model in upward flow that the presence of a liquid wall layer free of gas bubbles close to the wall, favours the onset of the downward directed secondary flow at the wall.

In microgravity conditions, bubbly flows have been mainly studied in the turbulent regime. The rate of coalescence in microgravity is much higher than in normal gravity upward or downward flow, especially when the bubble diameter is small compared to the tube diameter (Colin et al., 1991, 1996; Takamasa et al., 2003). In microgravity the relative velocity between the bubbles is often smaller than in normal gravity because the turbulence level is lower and there is no relative velocity induced by buoyancy. Thus the interaction time between the bubbles is larger in microgravity than in normal gravity and often sufficient to observe a complete drainage of the liquid film separating the two bubbles, leading to their coalescence. The void fraction profiles are rather flat across the tube section with a maximum close to the pipe center (Legendre et al., 1999; Takamasa et al., 2003). The wall shear stress in microgravity is comparable to single-phase flow or a little higher when the bubbles size is comparable to the channel diameter (Colin et al., 1996).

The aim of this paper is to present original results on a laminar bubbly flow in microgravity, especially concerning the wall shear stress, the bubble velocities and the evolution of their size due to coalescence. The experimental hardware described in Section 2 was built to operate aboard the sounding rocket Texus-45 launched from the European Space RANGE (North Sweden) in February 2008. The ballistic phase provided 6 min of microgravity with a level smaller than 10^{-4} g_0 (g_0 being the terrestrial gravity). All the results presented in this paper have been obtained during this flight. The experimental procedures are listed in Section 2 and the main results presented in Section 3. These results are discussed and compared to theoretical models in Section 4.

2. Experimental setup and procedure

2.1. Fluid loop and test cell

The experimental setup (Fig. 1) was built to operate aboard the sounding rocket TEXUS-45 and consists of a main liquid reservoir (1), a test channel (2), a compensation tube (3), a liquid supply tank (4), a gas storage tank (5), a nozzle (6), two gear pumps (PuTS, PuST), a peristaltic pump for the gas injection (PuGI), a flow meter and several valves for the flow control. The fluid temperature is measured at several locations (T_1, T_2 and T_3) via temperature sensors.

At the outlet of the test cell, the two phases are withdrawn and recirculated to the main reservoir, via the pump PuTS. The compensation tube defines the pressure boundary condition at the channel inlet and provides the volume balance of the gas injected into the loop. The pump PuST is used to adjust the fill level in the compensation tube, the liquid can be added or removed from the main liquid reservoir. Details of the setup and the operations are given by Salim et al. (2009).

The test channel (Fig. 2a) consists of two transparent parallel quartz plates of width $b = 25$ mm. The distance between these two plates is $a = 10$ mm. The flow along the length $l = 80$ mm is confined by a free surface on one side and a plate on the opposite side. The reference frame of the channel is displayed in Fig. 2b. Its origin is located in the middle of the cross section and at the beginning of the free surface.

The fluid enters into the capillary channel via a nozzle (6) which has an elliptical shape in the (x,y) plane but with no constriction in the (x,z) plane. The bubbles are injected at the nozzle level via six capillary tubes of 100 μm in inner diameter and 7.4 cm of length (Fig. 2b). These capillary tubes are connected to a manifold, which allows the repartition of the gas supplied by a peristaltic pump PuGI (Fig. 1) between the six capillary tubes. The placement of the capillary tubes, detailed in Table 1, is chosen in order to promote a homogeneous distribution of the bubbles at the channel entry. Due to the closed fluid loop, all bubbles crossing the capillary channel are kept in the main reservoir via the screens (element 7 in Fig. 1). Then, the liquid injected at the inlet of the capillary channel is free of bubbles.

The liquid FC-72 was chosen owing to its good wetting properties ($\sigma = 0.01$ N/m). The contact angle of a sessile liquid droplet on the quartz substrate is zero. The perfectly wetting liquid ensures a good pinning of the liquid at the edges of the channel. The density ρ of FC-72 is 1680 kg/m^3 and its dynamic viscosity is $\mu = 6.38 \ 10^{-4}$ Pa s. Nitrogen (N$_2$) is used to produce the bubbles. The liquid temperature at the inlet of the capillary channel is about 21 °C.

2.2. Flow visualisation and image processing

Three CCD cameras were used for flow visualisations. Two cameras (Sony XC ST 50) were focused on the channel (Fig. 2b). The resolution of the image was approximately 64.5 μm/pixel. Both sections of image had an overlap of about 3 mm. On the front plate markings were etched for the calibration of pictures and the check of the optical resolution. The third camera (Sony XC ST 70) was focused on the compensation tube.

The channel was illuminated from behind using a LEDs array emitting a light at a wavelength of 650 nm. The optical axes of the cameras were aligned perpendicularly to the quartz plates (Fig. 2b). The video signals were transmitted to ground by telemetry. The video material was digitized to 8-bit gray scale images. In order to determine the geometrical characteristics of the bubbles, the images were processed by using the software Optimas. Image processing consisted of:

(i) a division by a background image without bubbles that allows an increase in the contrast,
(ii) the application of a median filter in order to smooth the bubble contour,
(iii) the determination of the gray levels histogram,
(iv) the choice of a threshold on the gray levels, and a binarization,
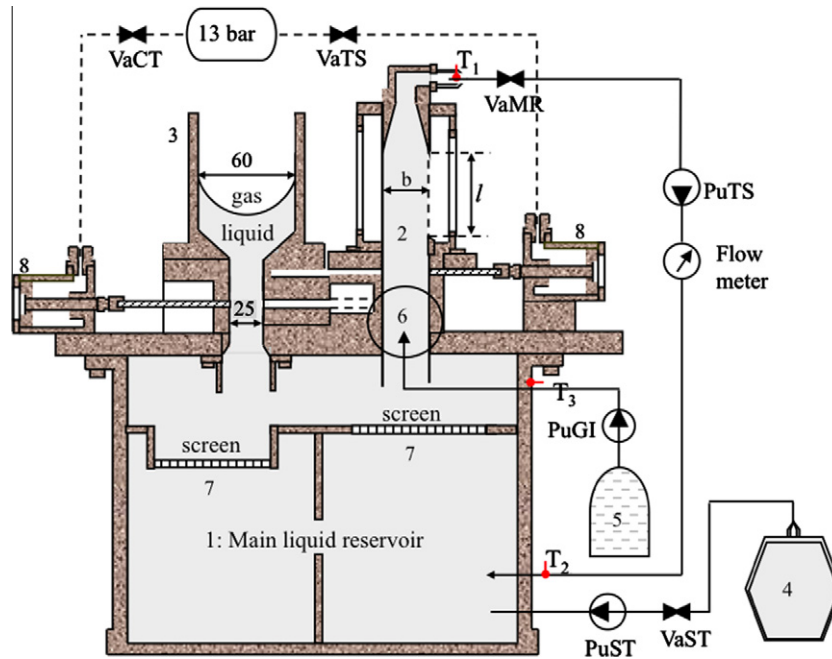(v) the detection of the bubble contour.

Fig. 1. Schematic drawing of the experimental setup: (1) main liquid reservoir, (2) test channel, (3) compensation tube, (4) liquid supply tank, (5) gas storage tank, (6) nozzle, (7) screens, (8) Valves, (PuST, PuTS) gear pumps, (PuGI) peristaltic pump for gas injection (T_1, T_2, T_3) temperature sensors.
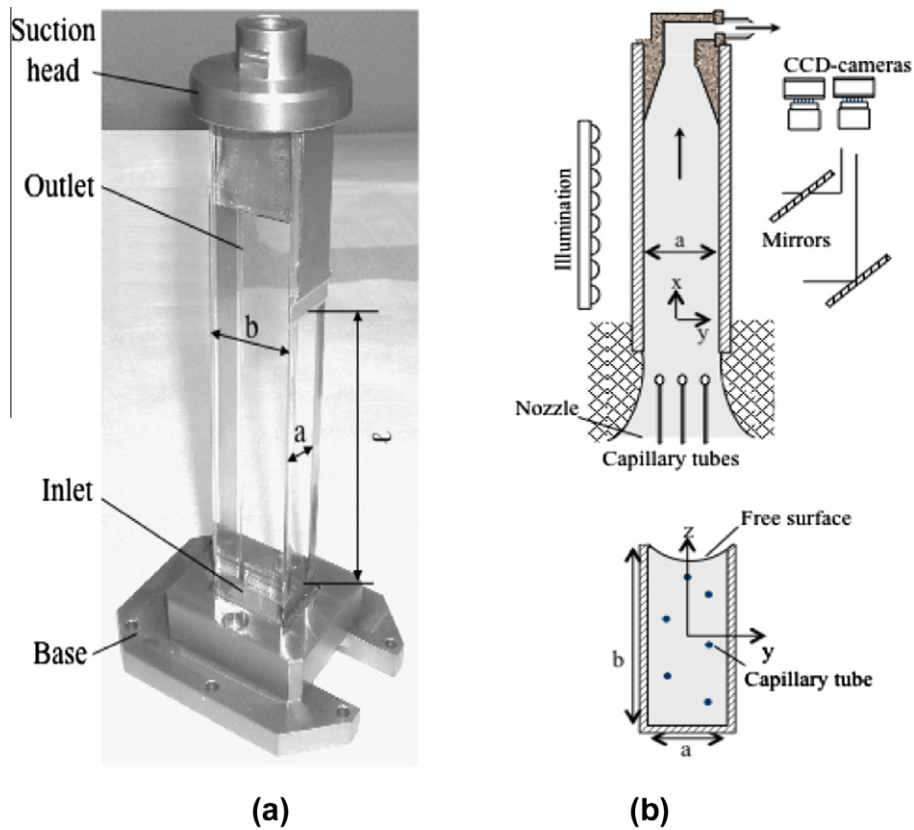

Fig. 2. Capillary channel, bubble injection device and optics.

The equivalent radius R and the center of gravity coordinates of each bubble were determined.

The liquid free surface contours were detected by looking for local maxima of the gradient of image intensity (Canny method) using Matlab software.

2.3. Experimental procedure

To avoid any leakage of the liquid during the launch of the rocket, the compensation tube and the open capillary channel were empty. The slide valves 8 (Fig. 1) were closed and the main reservoir was

Table 1
Detail of capillary tubes location in the nozzle for bubble injection (distances in mm).

Tube	1	2	3	4	5	6
x	−35	−35	−35	−35	−35	−35
y	−2.5	2.5	−2.5	2.5	−2.5	0
z	−8.75	−5	−1.25	2.5	5	7.5

Table 2
Liquid and gas flow rates and the corresponding duration.

Test	Q_m (ml/s)	Q_G (ml/s)	j_L (cm/s)	j_G (cm/s)	Period (s)
1	5.2 ± 0.02	0	2.08	0	
	5.2 ± 0.02	0.43 ± 0.02	1.91	0.17	17
2	5.2 ± 0.02	0.51 ± 0.02	1.88	0.20	19
3	5.2 ± 0.02	0.62 ± 0.03	1.83	0.25	27
	6.3 ± 0.02	0	2.5	0	
4	6.3 ± 0.02	0.62 ± 0.03	2.25	0.25	19.5

filled and free of bubbles. Once the microgravity conditions were achieved, the first slide valve 8 was automatically opened via VaCT and then the compensation tube was filled manually with the pump PuST (Fig. 1). This process was controlled remotely from the ground using the video and data downlink and the telecommand uplink. As soon as the compensation tube was filled up to a desired height, the liquid supply was interrupted and the slide valve 8 of the capillary channel was opened (via VaTS). Then, the liquid spread instantaneously into the test cell and formed a concave meniscus due to its good wettability with respect to the quartz material.

When the liquid meniscus reached the outlet of the capillary channel the valve VaMR was opened and the pump PuTS was started with the same flow rate as caused by the self-driven capillary flow (approximately 5 ml/s). Hence, the liquid was withdrawn by PuTS at a flow rate Q_L. When the steady state was reached the bubbles were injected at a given volumetric flow rate Q_G. During bubble injection the total flow rate $Q_m = Q_L + Q_G$ remained constant. The gas injection was stopped when the first bubbles reached the flow meter and then the gas elimination was started. This procedure was repeated several times with different liquid and gas flow rates during the microgravity duration. The sketch of the flight experiment is described in detail by Salim et al. (2009). Table 2 summarizes all explored liquid and gas flow rates with the corresponding duration. The liquid and gas superficial velocities j_L, j_G are also calculated assuming that the flow cross section is close to ab.

3. Experimental results

3.1. Liquid free surface contours

As described previously the bubbles are injected after reaching each steady state of single-phase flow, which is qualified by a stable liquid free surface. The pictures showing the observed configurations are presented in Figs. 3 and 4 for the explored flow rates. On the right part of the Figs. 3 and 4, we have also plotted the liquid free surface position, versus time, at a fixed point in the middle of the capillary channel ($x = l/2$, $y = 0$). These experimental results show that the free surface oscillation becomes more important in two-phase flows. A time period is needed for the flow stabilisation and a slight increase of the meniscus height in the compensation tube is induced.

The liquid free surface contours are extracted using image processing and averaged over a time period of about 2–3 s for each couple of liquid and gas flow rate. This last period is chosen with respect to the liquid free surface stability. The Figs. 5 and 6 represent the mean liquid free surface contours along the channel length for a total flow rate of 5.2 ml/s and 6.3 ml/s, respectively. In single-phase flow, the liquid free surface curvature increases with the liquid flow rate. In two-phase flow, the liquid free surface curvature diminishes as the injected gas flow rate increases. The decrease of the free surface curvature, which is more distinguished in Fig. 5, can be interpreted by an increase of the total volume of the fluid inside the capillary channel. Since the imposed flow rate of the pump PuTS is kept constant, the volume increase due to the gas injection (injected Q_G) is divided between the open capillary channel volume and the compensation tube to reach a hydrodynamic

equilibrium. The curvature of the free surface can be related to the local pressure in the flow and will be used to estimate the wall friction (see Section 4).

3.2. Bubble size evolution

Bubble diameters are determined by applying different image processing operations previously described. In order to analyse the coalescence rate, the diameters of the same bubble population are measured near the inlet ($x = 2.5$ mm) and the outlet ($x = 75$ mm) of the capillary channel. The number of bubbles in each region ranges between 100 and 400 depending on the flow parameters and the duration of the sequence. The diameter of each bubble d_i is determined from its projected area on the image assuming a spherical bubble shape. The bubble diameter distributions are plotted in Fig. 7 for the four test cases 1–4.

It is well known that the Probability Density Function (PDF) of bubble diameters frequently proves to be well presented by a log-normal distribution law (Kamp et al., 2001):

$$P(d) = \frac{1}{2\pi\hat{\sigma}d} \exp\left\{\frac{-[\ln(d/d_{00})]^2}{2\hat{\sigma}^2}\right\} \tag{1}$$

where d_{00} is the median diameter and $\hat{\sigma}$ a parameter characterising the width on the PDF. In order to fit the experimental bubble diameter distribution by a log-normal law, the parameters d_{00} and $\hat{\sigma}$ and all the characteristic diameters of the distribution can be calculated versus the moments S_γ of order γ of the PDF:

$$S_\gamma = n \int P(d)d^\gamma dd; \quad d_{\gamma\delta} = \left(\frac{S_\gamma}{S_\delta}\right)^{1/(\gamma-\delta)} = \left(\frac{\sum_{i=1,p}d_i^\gamma}{\sum_{i=1,p}d_i^\delta}\right)^{1/(\gamma-\delta)} \tag{2}$$

where n is the bubble number density. Using Eq. (2) d_{30} and the mean Sauter diameter d_{32} can be calculated and then d_{00} and $\hat{\sigma}$ are deduced (Kamp et al., 2001):

$$d_{00} = d_{30} \exp\left(-\frac{3}{2}\ln\left(\frac{d_{32}}{d_{30}}\right)\right); \quad \hat{\sigma} = \sqrt{\ln\left(\frac{d_{32}}{d_{30}}\right)} \tag{3}$$

The log-normal laws are also plotted in Fig. 7. For test cases 1 and 4, the experimental PDF is well fitted by a log-normal law. Due to the very short length of the channel and also multiple coalescences of the same bubbles, some deviations of the PDF with a log-normal law can be observed (tests 2 and 3). Nevertheless, the values of d_{00} and $\hat{\sigma}$ are also calculated in these cases. In Table 3, the characteristic parameters of the bubble diameter distributions are gathered. Despite the small length of the channel, coalescence seems very efficient to increase the bubble size. The bubble size evolution along the channel will be compared in Section 4 to the prediction of a theoretical model previously developed for bubbly flow in microgravity (Colin et al., 2008).

3.3. Bubble velocities

From image processing it is also possible to determine the bubble velocity. Since the video cameras took pictures of the plane (x,
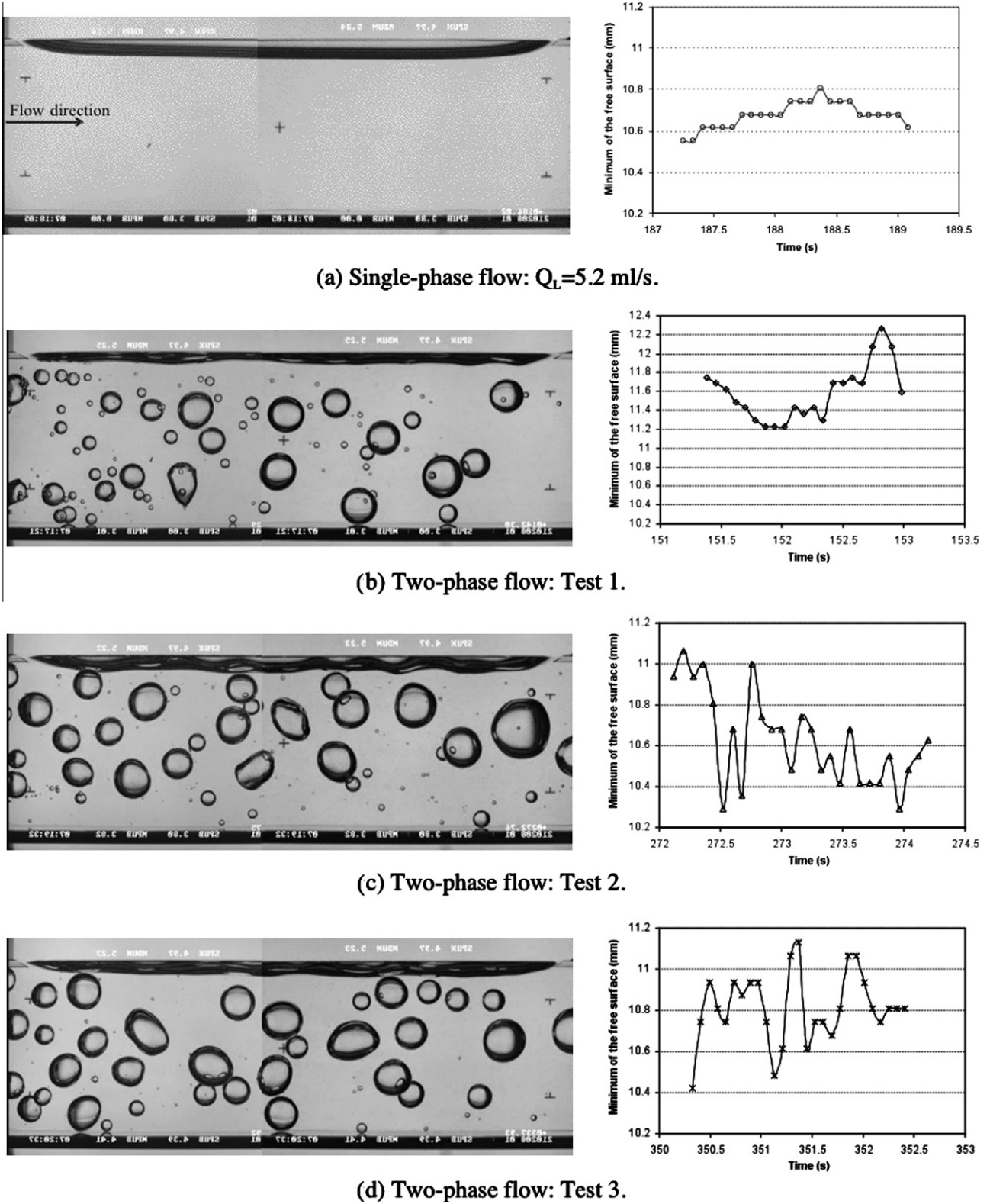
(a) Single-phase flow: Q_L=5.2 ml/s.

(b) Two-phase flow: Test 1.

(c) Two-phase flow: Test 2.

(d) Two-phase flow: Test 3.

Fig. 3. Photographs of the observed flow and displacement of the middle point ($x = 40$ mm, $y = 0$ mm) of the liquid free surface contours, for a total flow rate $Q_m = 5.2$ ml/s.

z), the velocities correspond to bubbles located in different y locations from -5 mm to 5 mm. The bubbles are initially injected at different locations $y = -2.5$ mm, 0 mm and 2.5 mm (see Fig. 2b and Table 1). The bubble velocities are calculated by measuring the position of the bubble in two consecutive images separated by a time interval of $\Delta t = 0.08$ s. The velocities are measured at the channel inlet ($x = 2.5$ mm), at the mid-length ($x = 40$ mm) and at the outlet ($x = 75$ mm).
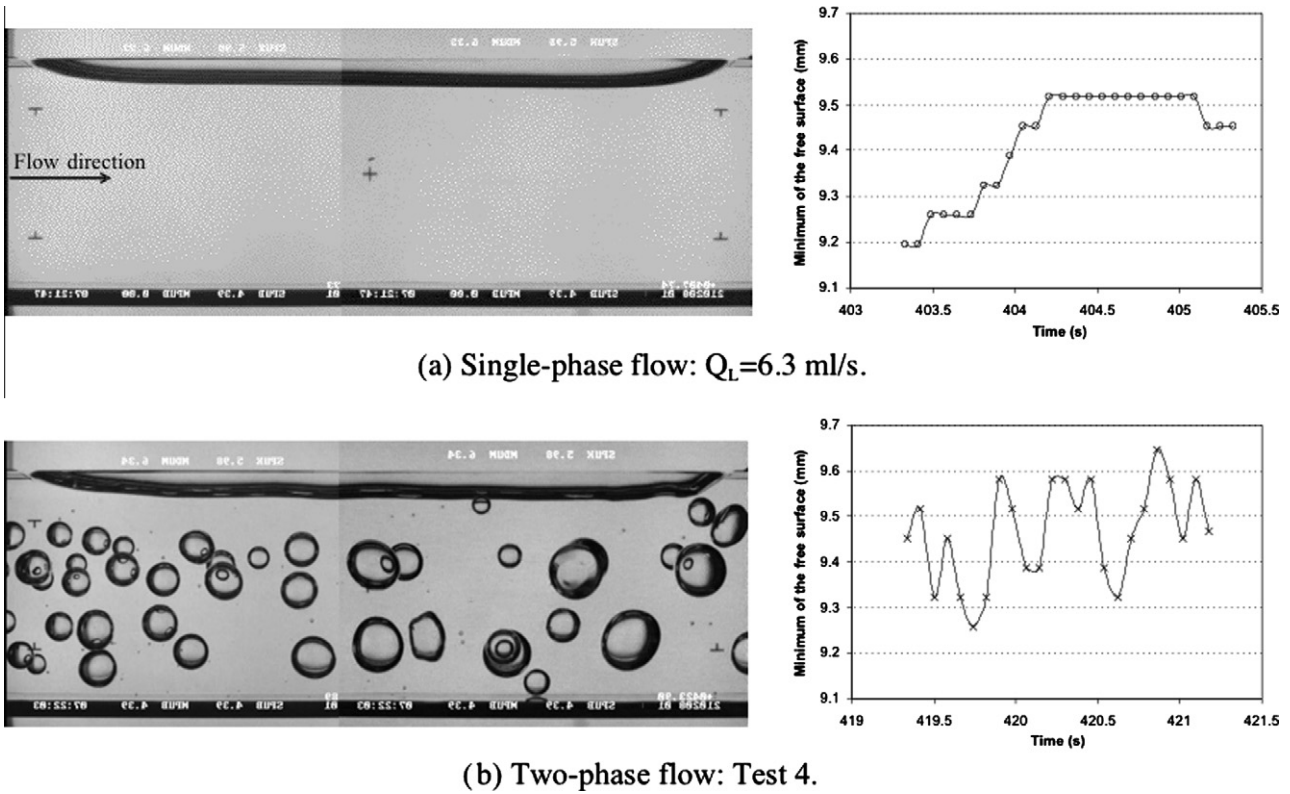
(a) Single-phase flow: Q_L=6.3 ml/s.

(b) Two-phase flow: Test 4.

Fig. 4. Photographs of the observed flow and displacement of the middle point (x = 40 mm, y = 0 mm) of the liquid free surface contours, for a total flow rate Q_m = 6.3 ml/s.
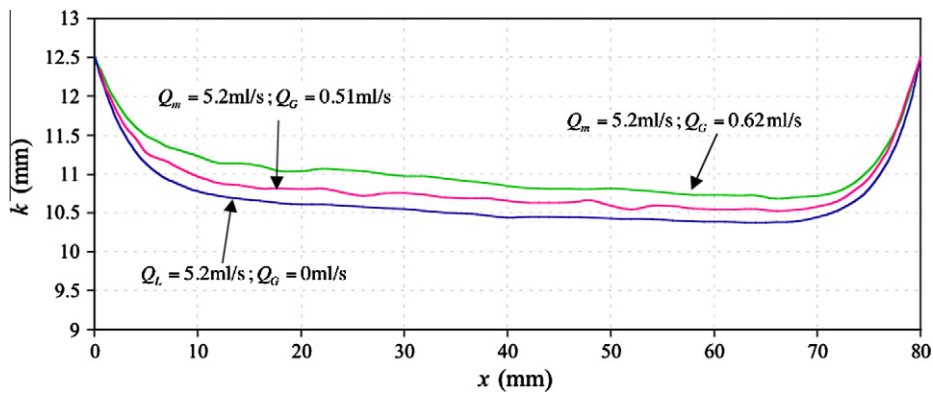

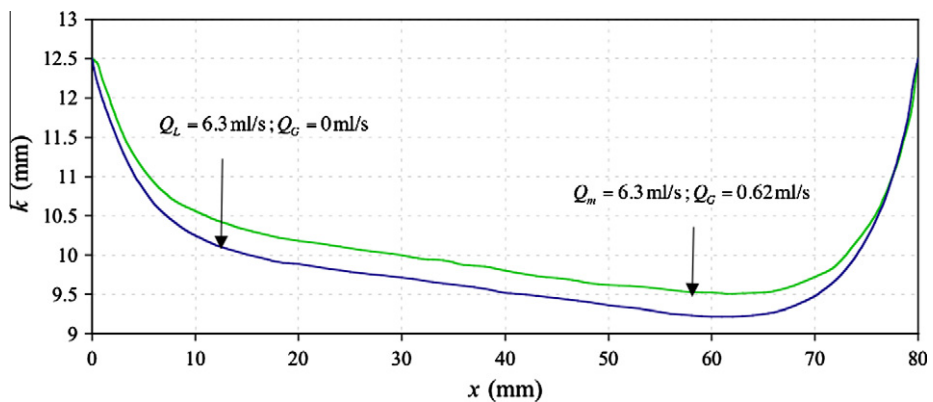Fig. 5. Effect of the bubbles on the liquid free surface profile k for a total flow rate of 5.2 ml/s.

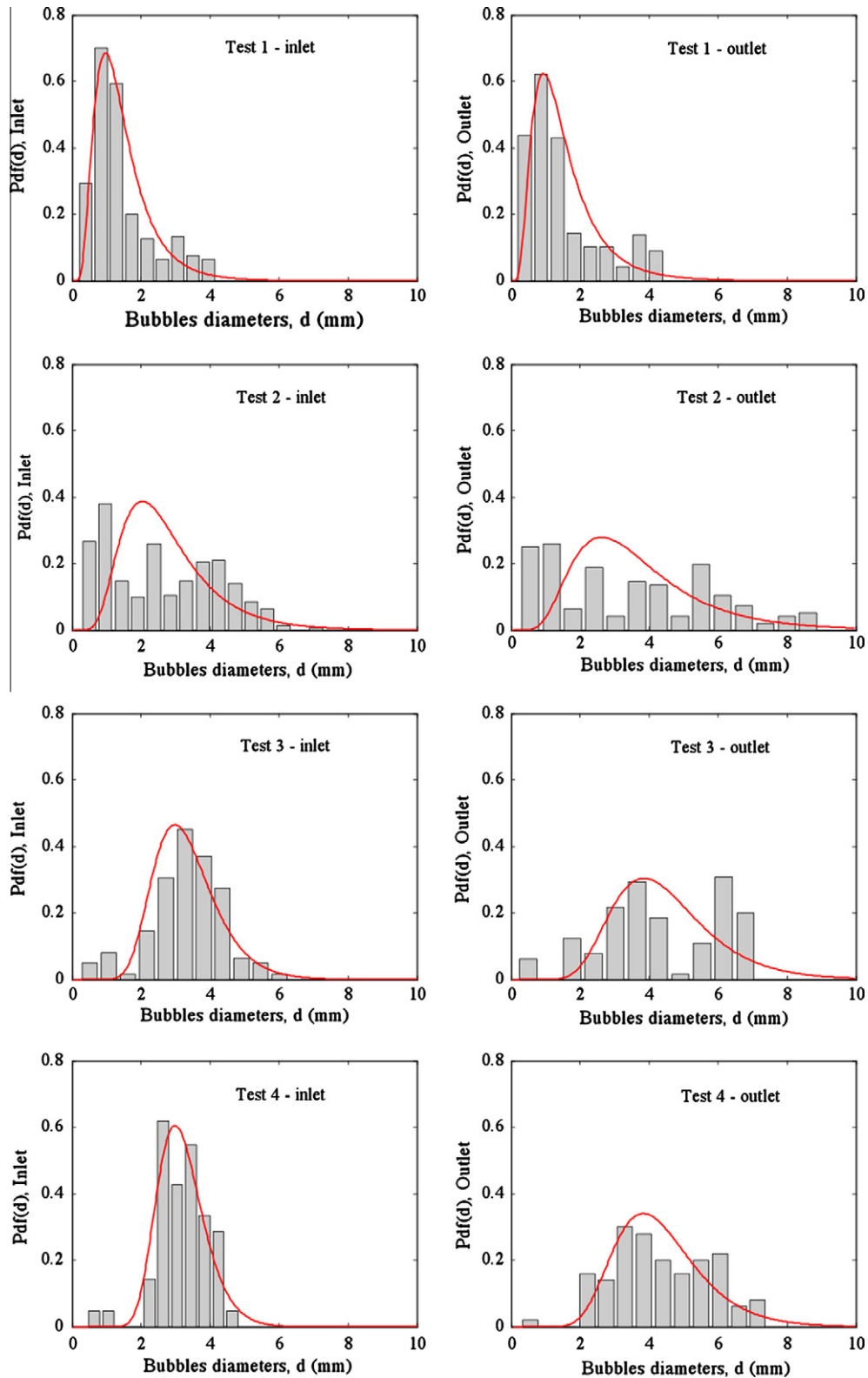Fig. 6. Effect of the bubbles on the liquid free surface profile k for a total flow rate of 6.3 ml/s.

Fig. 7. PDF of the bubble diameters at the inlet and the outlet of the capillary channel.

In Fig. 8, the velocity of each bubble U_b is plotted for the outlet test section (x = 75 mm) versus its position in z-direction for test cases 2 and 3 (Fig. 8a) and test case 4 (Fig. 8b). In these figures, the velocity profiles of the liquid for y = 0 and 2.5 and 4 mm are also plotted. These velocity profiles have been calculated by numerical simulation using the CFD code Flow 3D. The laminar liquid flow is simulated from the converging test section to the outlet of the channel. The boundary condition imposed at the free surface is a no-shear condition. The deformation of the free surface is not calculated. This means that

Table 3
Characteristic bubble diameters at inlet and outlet of the channel.

Test	Inlet			Outlet		
	d_{00} (mm)	$\hat{\sigma}$	d_{32} (mm)	d_{00} (mm)	$\hat{\sigma}$	d_{32} (mm)
1	1.23	0.54	2.54	1.32	0.57	3.04
2	2.39	0.48	4.25	2.92	0.54	5.98
3	3.21	0.28	3.90	4.20	0.33	5.55
4	3.12	0.22	3.51	4.13	0.31	5.24

the curvature of the free surface due to the difference between the liquid and the ambient pressures is not considered. This assumption has a negligible effect on the value of the flow cross section (<2%). Thus it is a good approximation, which allows obtaining a stable velocity profile in the x–z plane. Otherwise, the liquid velocity profile is unstable due to the free surface oscillation.

The bubble velocities are distributed around the value of the liquid velocity at $y = 2.5$ mm. It can be explained by two main reasons: (i) most of the bubbles are injected at the position $y = \pm 2.5$ mm and do not deviate much from this position along the channel, (ii) the bubble slip velocity is expected to be very weak in microgravity. The bubbles whose velocities are close to the liquid velocity for $y = \pm 2.5$ mm are therefore close to this position. The small deviation of the bubble trajectory in y-direction may be explained by the short length of the test section, but also by the absence of a lift force acting on the bubble in microgravity.
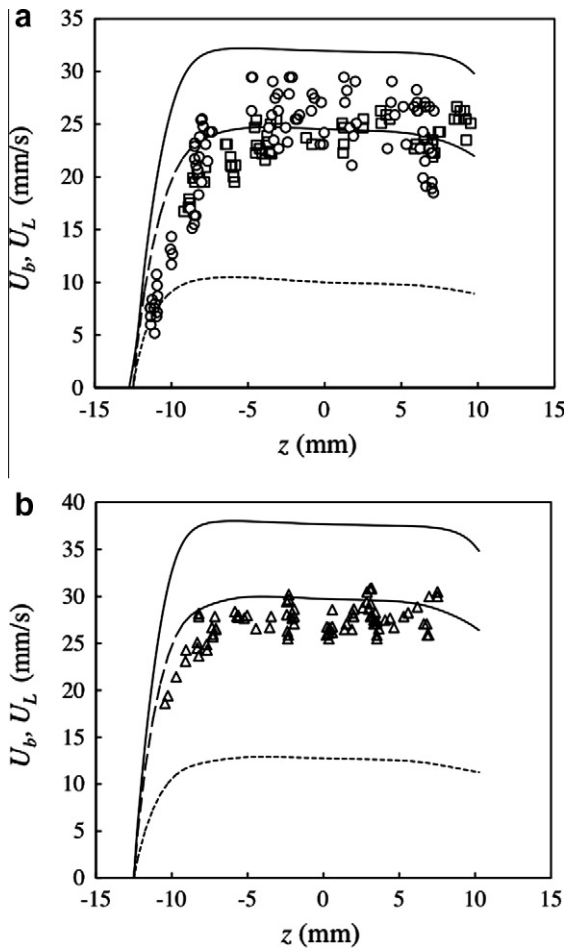

Fig. 8. Bubble and liquid velocities at the outlet of the channel Measured bubble velocities U_b-circle: test 2, square: test 3, triangle: test 4 Computed liquid velocities U_L: solid line $y = 0$, dashed line $y = 2.5$ mm, dotted line $y = 4$ mm.
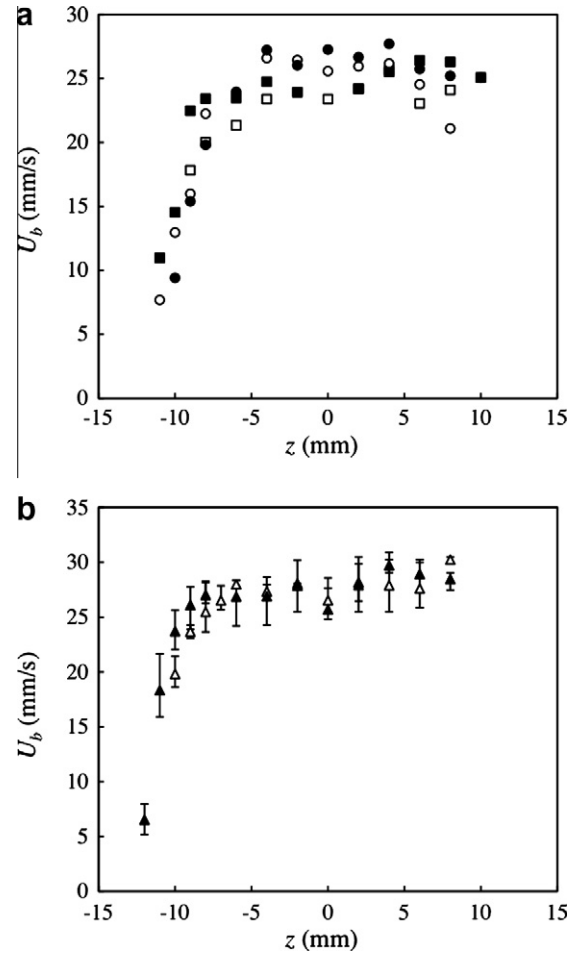

Fig. 9. Bubble velocities averaged in the y-direction – filled symbols: inlet test section – open symbols: outlet test section circles: test 2 – squares: test 3 – triangle: test 4.

The bubble velocities averaged in the y-direction are also calculated for different z values. An interval of $\Delta z = 1$ mm (close to the wall) or 2 mm around z is chosen for averaging the velocity. The mean bubble velocities at the inlet and outlet of the channel are plotted in Fig. 9a for $Q_m = 5.2$ ml/s and in Fig. 9b for $Q_m = 6.3$ ml/s. The maximum and minimum values of U_b are also plotted for $Q_m = 6.3$ ml/s. For better readability they are not plotted for $Q_m = 5.2$ ml/s. The mean bubble velocity slightly evolves between the inlet and outlet of the channel because of the change in the cross section A.

4. Discussion

4.1. Mean bubble velocity and void fraction

From image processing the bubble velocities have been measured at different distances x from the channel entrance. Then the bubble velocities are averaged across the flow section A to obtain the mean gas velocity U_G. The cross section of the flow also evolves along the flow and can be calculated versus $k(x)$, the distance of the free surface to the mid-plan of the channel ($z = 0$). Following Haake et al. (2006), two situations can be observed. The liquid can be pinned at the edge of the channel when $k > (b - a)/2$, or the liquid separates from the edge of the channel when $k < (b - a)/2$. Then two expressions for $A(x)$ can be derived:
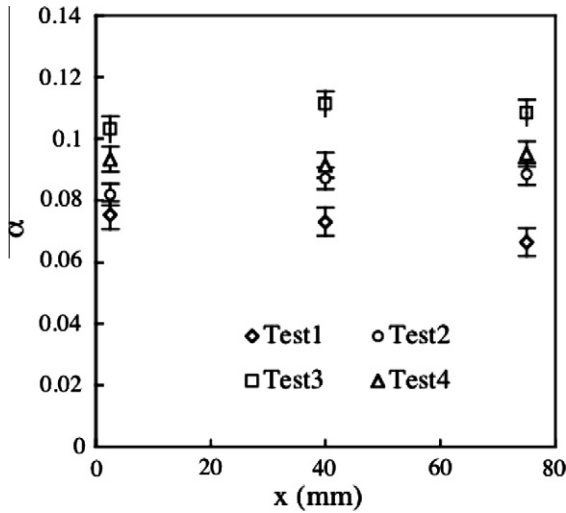
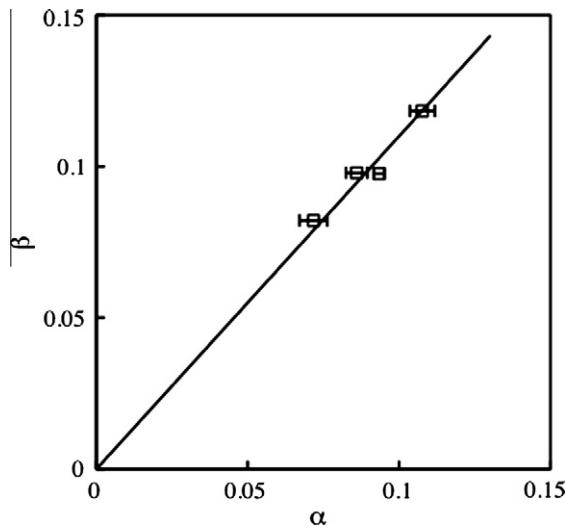**Fig. 10.** Mean void fraction measurements along the channel.

Fig. 11. Injection ratio versus mean void fraction solid line: $\beta = 1.1 \alpha$.

$$A(x) = ab \left[1 - \frac{R^2}{ab} \arcsin \left(\frac{a}{2R} \right) + \frac{R - b/2 + k}{2b} \right] \quad \text{with}$$

$$R = \frac{a^2 + (b - 2k)^2}{4(b - 2k)^2} \quad \text{if } k \geqslant \frac{b - a}{2}$$

$$A(x) = \frac{ab}{2} + \frac{a^2}{2} \left[\frac{2k}{a} + 1 - \frac{\pi}{4} \right] \quad \text{if } k < \frac{b - a}{2} \tag{4}$$

In our experiments, we are always in the configuration of a liquid free surface pinned at the edge of the channel, k is always larger than 7.5 mm. From the measured values of the mean gas velocity $U_G(x)$ and the cross section $A(x)$, it is possible to calculate the mean void fraction α:

$$\alpha = \frac{Q_G}{U_G A}$$

In Fig. 10 the values of the void fraction are plotted for different positions x. From the experimental results we can consider that the void fraction is almost constant along the channel within the measurement uncertainties. For each test case, a mean value of the void fraction is then calculated and the injection ratio $\beta = Q_G/Q_m$ is plotted versus this value for the four test cases in Fig. 11.

The horizontal error bars in the figure correspond to the difference in the void fraction values for the three x-positions. A linear dependency of β with α is observed, that is in good agreement with the classical gas velocity law found in turbulent bubbly pipe flows in microgravity (Colin et al., 1991, 1996):

$$\beta = C_0 \alpha \Longleftrightarrow U_G = C_0 U_m \quad \text{with } U_m = \frac{Q_m}{A} \tag{6}$$

The value of the coefficient C_0 is equal to 1.1. It depends on the velocity profile and on the local void fraction distribution (Zuber and Findlay, 1965). If we consider a parabolic velocity profile in the y-direction, $U_L(y,z) = 1.1\ U_m$ is obtained for $y = \pm 2.6$ mm, which is close to the y position where the bubbles are injected. The memory of the location where the bubbles have been created is therefore very high due to the short channel length.

4.2. Bubble coalescence modelling

To predict the evolution of bubble size along the tube, a mechanistic model was developed (Kamp et al., 2001). Its starting point consists of the transport equation of the PDF of bubble diameters $P(d)$. Usually this Liouville-like equation is solved after discretizing the function $P(d)$ into several classes: this is the so-called "population balance method". In the present study we used a different approach that will be justified below. The statistical function $P(d)$ may be approximated by a truncated series of statistical moments defined by Eq. (2). Then a transport equation for each moment can be written:

$$\frac{\partial S_\gamma}{\partial t} + \nabla \cdot (u_G S_\gamma) = \phi_\gamma \tag{7}$$

The lhs of Eq. (7) accounts for the transport by the gas velocity u_G while the rhs is a source term due to coalescence and break-up. Break-up was not observed in our microgravity experiments, suggesting that the bubble size evolves only by coalescence.

The model is applied assuming that the PDF of the bubble diameters is well fitted by a log-normal law given by Eq. (1). But the results of the model are not very sensitive to the shape of the PDF (log-normal, gamma function) chosen for the calculation of the moments. Despite the discrepancy between the experimental PDF and the log-normal law observed for test cases 2 and 3, the model will be used assuming the PDF given by a log-normal law. Thus any moment is a function of the two parameters d_{00} and $\hat{\sigma}$. The interest of the method relies on the needs of only two moments (e.g. S_1 and S_2) for determining d_{00} and $\hat{\sigma}$. Eq. (7) has to be solved for example for S_1 and S_2. Thus the two parameters d_{00} and $\hat{\sigma}$ as well as the mean Sauter diameter d_{32} are algebraic functions of S_1 and S_2:

$$\hat{\sigma} = \left[\ln \left(\frac{6\alpha S_1}{\pi S_2^2} \right) \right]^{1/2} ; \quad d_{00} = \frac{6\alpha}{\pi S_2} e^{-5\hat{\sigma}^2/2}; \quad d_{32} = \frac{6\alpha}{\pi S_2} \tag{8}$$

To solve Eq. (7), we have to model ϕ_γ, the rate of change of S_γ resulting from the coalescence process. This term can be modelled as the product of the coalescence probability P_c by the collision frequency dC for two bubbles of diameters d_1 and d_2 (Kamp et al., 2001):

$$\phi_\gamma = \frac{1}{2} \int_{d_1=0}^{\infty} \int_{d_2=0}^{\infty} P_c(d_1, d_2) \left[(d_1^3 + d_2^3)^{\gamma/3} - d_1^\gamma - d_2^\gamma \right] dC(d_1, d_2)$$

$$\text{with} \quad P_c = \exp \left[-K_P \sqrt{\frac{\rho_L V^2 2 d_1 d_2}{C_{vm} \sigma (d_1 + d_2)}} \right] ;$$

$$dC(d_1, d_2) \approx K_C n^2 P(d_1) P(d_2) \left(\frac{d_1 + d_2}{2} \right)^2 V(d_1, d_2) dd_1 dd_2 \tag{9}$$
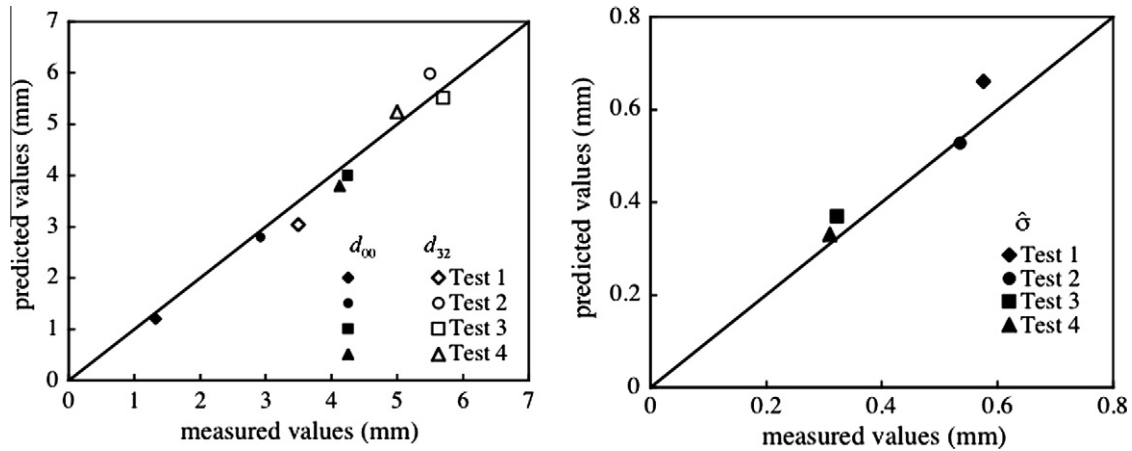
Fig. 12. Prediction of the parameters of the log-law and the mean Sauter diameter at the channel outlet- left filled symbols: d_{00} open symbols d_{32}, right $\hat{\sigma}$.

where ρ_L and σ are the liquid density and the surface tension, respectively. C_{vm} is a virtual mass coefficient for two touching bubbles of equal sizes and equal to 0.803 (Kamp et al., 2001). K_P and K_C are two constants of the model of order 1. V is the relative velocity of two bubbles. Since the flow is laminar, the relative velocity of two bubbles is mainly controlled by the mean shear rate G (Colin et al., 2008):

$$V(d_1, d_2) = \frac{G}{\sqrt{2C_{vm}}}\left(\frac{d_1 + d_2}{2}\right) \tag{10}$$

In order to achieve the comparison with the experimental data, Eq. (7) is averaged over the channel cross section. It is thus necessary to define an averaged value of G over the channel section. The experimental observations showed that the bubble coalescence is mainly controlled by the velocity gradient in the y-direction. If we consider a parabolic velocity profile in the x–y-plane, the mean velocity gradient is equal to $2 U(x,0,z)/a$ for half of the channel. But this value should not be averaged over all the channel depth, since the collisions between bubbles of diameters d_1 and d_2 do not occur in the wall vicinity at a distance smaller than the bubble radius. Excluding this region, G averaged over the channel cross section becomes:

$$G = \frac{3U_m}{2}\frac{2}{a}\left[1 - \frac{2}{a}\min\left(\frac{d_1}{2}, \frac{d_2}{2}\right)\right]^2 \tag{11}$$

The velocity scale V calculated using Eqs. (10) and (11) is then introduced in Eq. (9) and ϕ_γ is numerically calculated using the Matlab software.

For a steady flow, Eq. (7) is integrated over the channel cross section:

$$\frac{1}{A}\frac{d}{dx}(U_G A S_\gamma) = \overline{\phi_\gamma} \tag{12}$$

Eq. (12) coupled with Eq. (8) is numerically solved for $\gamma = 1$ and $\gamma = 2$ and the axial evolution of S_1, S_2, d_{00} and $\hat{\sigma}$ along the channel is calculated. The inlet conditions for the simulations are the values of d_{00} and $\hat{\sigma}$ obtained by fitting the experimental PDF at the channel inlet (Table 3). In Fig. 12, the predicted values of d_{00}, $\hat{\sigma}$ and the Sauter diameter d_{32} at the channel outlet are plotted versus the experimental values. The best agreement between the model and experiments is obtained using the value $K_P = 2$ and $K_C = 1.2$.

The coalescence model initially developed to predict turbulence induced bubble coalescence and extended to shear-induced coalescence is thus also able to predict the high coalescence rate observed in a laminar flow in microgravity.

4.3. Pressure drop and wall friction

In order to estimate the wall friction from the free surface curvature, the model developed by Rosendahl et al. (2004) for single-phase flow will be extended to two-phase flows. In single-phase flow in microgravity for a constant volumetric flow rate Q_L, the momentum balance equation can be written:

$$\frac{1}{A(x)}\frac{d}{dx}\left(\rho_L\frac{Q_L^2}{A(x)}\right) = -\rho_L\frac{Q_L^2}{A^3(x)}\frac{dA(x)}{dx} = -\frac{dP}{dx} - \frac{P_w}{A(x)}\tau_w \tag{13}$$

where $A(x)$ is the local flow cross section, $P_w = 2b + a$, the wetted perimeter of the channel and τ_w the wall shear stress. The interfacial shear stress at the free surface is equal to zero. In single-phase flow, the wall shear stress can be expressed as:

$$\tau_w = \frac{1}{2}\rho_L\frac{Q_L^2}{A^2}\left(\frac{K_f}{Re_L}\right) \quad \text{with } Re_L = \frac{4Q_L}{P_w\nu_L} \tag{14}$$

where K_f/Re_L is the friction factor. If we consider that an open channel with an aspect ratio $b/a = 2.5$ is equivalent to a close channel with an aspect ratio of 5, the friction factor for a developed laminar flow would be equal to $76.26/Re_L$ (White, 1986).

The pressure gradient in Eq. (13) can be calculated from the curvature of the free surface. Assuming zero normal and tangential stresses at the liquid free surface and a passive overlaying gas, the capillary pressure is related to the free surface curvature by the Gauss–Laplace equation:

$$P - P_a = -\sigma\left(\frac{1}{R_1} + \frac{1}{R_2}\right) = -\sigma h \tag{15}$$

where P_a is the ambient pressure, $h/2$ the mean curvature of the liquid surface, R_2 is the main curvature radius in the flow direction x and it is perpendicular to R_1. Following Rosendahl et al. (2004), R_1 and R_2 can be related to $k(x)$, the position of the free surface at the symmetry plane of the channel ($y = 0$) and its derivatives:

Table 4
Values of K_1, K_2 and K_3 according to different investigated flow rates.

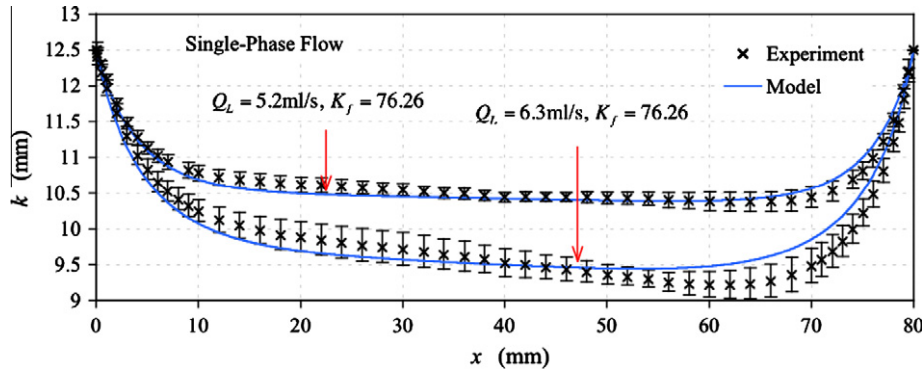|		K_1 (cm^{-7} s^2)	$K_2 \times 10^{-4}$ (cm^{-4} s)	K_3 (cm^{-1})
Single-phase flow	$Q_L = 5.2$ ml/s	5.73	1.18	0.67
	$Q_L = 6.3$ ml/s	5.73	1.18	0.67
Two-phase flow	Test 2	4.65	0.96	0.67
	Test 3	1.4	0.65	0.67
	Test 4	4.02	0.8	0.67

Fig. 13. Free surface contour for single-phase flow: comparison of the measurements with the calculated profiles.
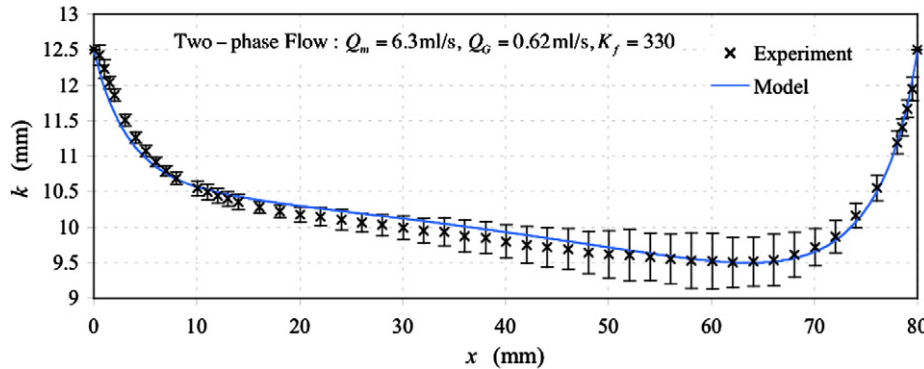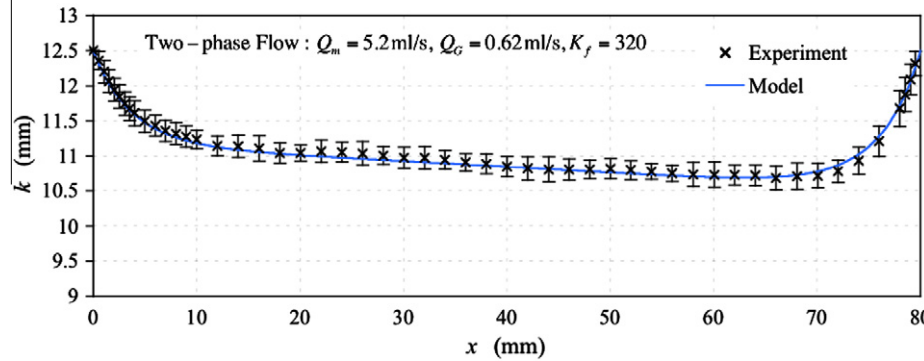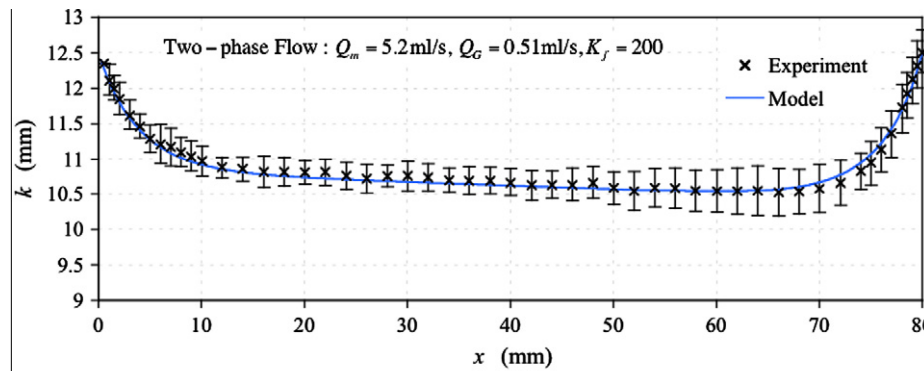

Fig. 14. Free surface contours for two-phase flow: comparison of the measurements with the calculated profiles.

$$R_1 = \begin{cases} \frac{a}{2}\left(\frac{1+d^{*2}}{2d^*}\right) & \text{if } d^* < 1 \text{ with } d^* = \frac{b-2k}{a}\left[1+\left(\frac{dk}{dx}\right)^2\right]^{1/2} \\ \frac{a}{2} & \text{if } d^* \geqslant 1 \end{cases} \quad (16)$$

The first value of R_1 is valid when the free surface is pinned to the channel edge. When the free surface is detached from the channel, then the radius R_1 is equal the half depth of the channel. The
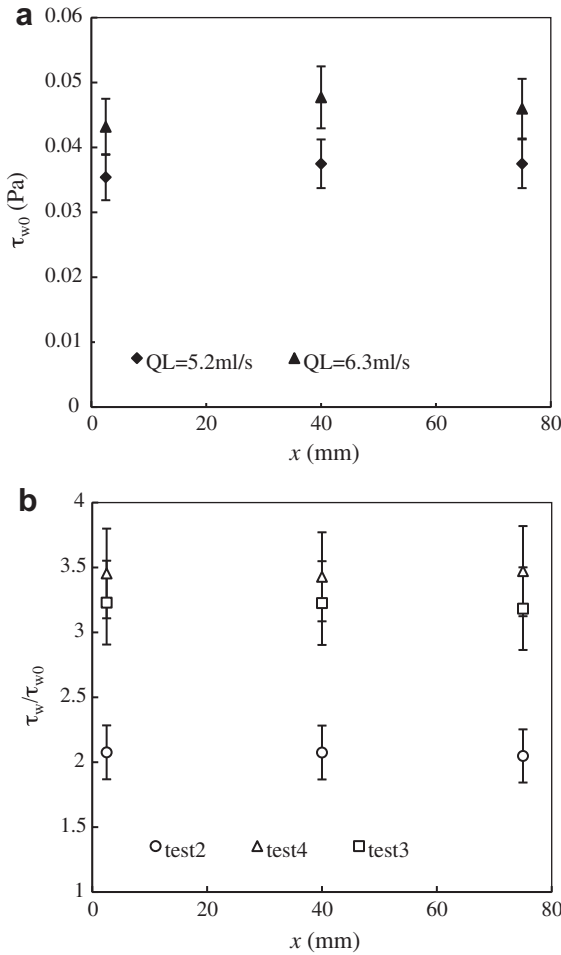
Fig. 15. Wall shear stress at different locations of the channel in single-phase flow (a) and ratio of the wall shear stress in two-phase flow and in single-phase flow (b).

detachment of the free surface from the channel can occur in the case of a bad wetting liquid. In this case, the three phase (gas–liquid–solid) contact line detaches from the edges of the channel and $k(x)$ is not be equal to 12.5 mm for $y = -a/2$ and $y = a/2$, but lower.

The calculation of the local curvature from experimental data is not an easy task because the position of the free surface oscillates and the errors in the calculation of the derivatives values of k are amplified. This is the reason why experimental data are directly compared to the theoretical profile of the free surface. The expression of the mean curvature (Eq. (16)) is replaced in Eq. (15). Then the pressure gradient is calculated and introduced in Eq. (13), which is integrated twice to obtain the profile $k(x)$.

In all investigated flow rates, the liquid free surface is pinned at the edges of the channel inlet and outlet due to the good wetting property of the used liquid (FC-72). Then, at the inlet and outlet of the capillary channel k is equal to 12.5 mm and the slope at the channel entrance is given by the pressure at the channel inlet $P_0(x = 0)$. In fact, the surface curvature at the channel inlet h_0 is defined by the capillary pressure of the meniscus in the compensation tube plus the convective and the frictional flow pressure losses inside the main liquid reservoir (1) and the nozzle (6) (see more details in Haake et al., 2006). Then, h_0 can be expressed as:

$$h(x = 0) = h_0 = K_1 Q^2 + K_2 Q + K_3 \quad \text{with} \quad K_3 = \frac{2}{R_{CT}} \tag{17}$$

where R_{CT} is the compensation tube radius and is equal to 3 cm, Q is the volumetric liquid flow rate. The values of K_1, K_2 and K_3 are given in Table 4.

In Fig. 13, the free surface curvatures measured in single-phase flow are compared to the calculated values for $K_f = 76.26$. An oscillation of the free surface is observed and the maximal and minimal positions of the free surface are included in the error bars in this figure. A good agreement between experiments and calculation is then observed for $Q_L = 5.2$ ml/s. For $Q_L = 6.3$ ml/s, the flow rate is close to the critical flow rate above which gas ingestion in the channel occurs. The curvature of the free surface becomes higher near the channel outlet.

This procedure is well validated for single-phase flows. The theoretical value of $K_f = 76.26$ is in good agreement with the experimental data. No further validation of the model is possible because the theoretical value of the wall shear stress is only known in single-phase flow.

The model will be now extended to bubbly flow in microgravity in order to estimate the value of K_f and to compare it to single-phase flow. In two-phase flow, the momentum balance for the mixture may be written:

$$\frac{1}{A}\frac{d}{dx}\left[\frac{\rho_G Q_G^2}{\alpha A} + \frac{\rho_L Q_L^2}{(1-\alpha)A}\right] = -\frac{dP}{dx} - \frac{P_w \tau_w}{A} \tag{18}$$

where Q_G and Q_L are constant, α is the mean void fraction in a cross section which was determined from the mean bubble velocity (see Section 4.1). In the experiments it was found that α remains constant along the channel. Then introducing the total flow $Q_m = Q_G + Q_L$ and the injection ratio $\beta = Q_G/Q_m$, Eq. (18) becomes:

$$-\frac{1}{A^3}\left[\frac{\rho_G \beta^2}{\alpha} + \frac{\rho_L(1-\beta)^2}{(1-\alpha)}\right]Q_m^2\frac{dA}{dx} = -\frac{1}{A^3}\rho_m Q_m^2\frac{dA}{dx} = -\frac{dP}{dx} - \frac{P_w \tau_w}{A} \tag{19}$$

where ρ_m is the density of the equivalent mixture. A similar equation to Eq. (13) is thus obtained with the following modelling of the wall shear stress:

$$\tau_w = \frac{1}{2}\rho_m\frac{Q_m^2}{A^2}\left(\frac{K_f}{Re_m}\right) \quad \text{with} \quad Re_m = \frac{4Q_m}{P_w \nu_L} \tag{20}$$

As for single-phase flow, the value of K_f includes the entrance effects. Using Eqs. (15), (16), and (20), Eq. (19) is integrated to calculate the shape of the free surface. The calculations are compared to the experiments in Fig. 14. The values of K_f are larger in two-phase flow than in single-phase flow. From these data it is then possible to estimate the increase in the wall shear stress in two-phase flow by comparison to single-phase flow. Note that the constant K_f highly depends on the slope of the liquid free surface. Even the first two curves in Fig. 14 (which correspond to the tests 2 and 3, respectively) seem to be similar, but the slopes are different. The value K_f is reflected by the slope of the liquid free surface. In Fig. 14 for $Q_m = 6.3$ ml/s and $Q_G = 0.62$ ml/s, the value of K_f for the maximum ends of errors bars is about 260 and the value of K_f corresponding to the minimum of ends of errors bars is about 380.

The total values of the wall shear stress τ_w are plotted in Fig. 15. The errors bars were obtained from the calculation of a maximum and a minimum factor K_f corresponding to the upper and lower liquid free surface presented in Fig. 14 by the errors bars. These values are very low, of the order or 0.1 Pa and almost constant along the channel. For test 2 corresponding to a void fraction of 0.08, the wall shear stress is about twice the value in single-phase flow. This value is even more important for test 3 with a void fraction of 0.11. The increase in the wall shear stress in two-phase flow is also very high for test 4 with a similar value of the void fraction 9% but a

higher liquid velocity. The reason of such an increase is not clear. It is interesting to point out that even in microgravity without a slip velocity between the bubbles and the liquid, a significant increase in the wall shear stress can be observed in two-phase flow. In these experiments the bubble diameter may reach a value of 7 mm, which is close to the channel thickness. So even without a slip velocity they may disturb the liquid flow in the wall vicinity.

5. Conclusion

An experimental investigation of a bubbly two-phase flow in an open capillary under microgravity conditions was presented. Two different liquid flow rates and three different gas flow rates led to different volumetric gas flow rate ratios. Millimetric bubbles were injected via six capillary tubes at the channel inlet.

A high coalescence rate was observed along the flow path. The bubbles often coalesced several times (multiple coalescence) due to their surface oscillations after the first coalescence.

The effect of the bubbles on the liquid free surface was observed. Experimental results exhibited the existence of a transition period before a hydrodynamic equilibrium between the liquid free surface and the compensation tube meniscus. This was due to a fixed flow rate at the outlet of the capillary channel but the volume from the additional gas injection is divided between the capillary channel and the compensation tube volume resulting in a motion of the liquid free surface.

After processing of the flow pictures, it was possible to measure the bubble sizes and velocities along the channel. The mean gas velocity was proportional to the mixture velocity $U_G = C_0 U_m$, with a parameter C_0 function of the bubble distribution in the channel. The value of C_0 pointed out that the position of the bubbles in the cross section was roughly the same at the inlet and outlet of the channel. Due to the short length of the channel and the absence of a lift force in microgravity, the transverse motion of the bubbles was very weak.

The bubble size strongly evolved along the channel due to a high rate of coalescence. The coalescence is induced by the collision of the bubbles in the shear flow. The bubble size evolution along the channel was calculated by using the theoretical model developed by Kamp et al. (2001) for two-phase flow in microgravity. In this model a velocity scale based on the mean shear of the flow was introduced to calculate the rate of coalescence. The prediction of the model compared very well with the experiments.

Since the curvature of the free surface was directly related to the local pressure, it was possible to access to the wall shear stress. For a given value of the wall friction coefficient the evolution of the curvature of the free surface was calculated using the theoretical model developed by Rosendahl et al. (2004). The value of the wall friction coefficient was adjusted by the comparison with the experimental free surface profile. This model has been extended to two-phase flow by solving the momentum balance equation for the mixture. Finally the wall shear stress in two-phase flow was compared to that in single-phase flow. Despite the absence of a bubble slip velocity in microgravity, the wall shear stress highly increased in two-phase flows.

References

Azpitarte, O.E., Buscaglia, G.C., 2003. Analytical and numerical evaluation of two-fluid model solutions for laminar fully developed bubbly two-phase-flows. Chem. Eng. Sci. 58, 3765–3776.

Biswas, S., Esmaeeli, A., Tryggvason, G., 2005. Comparison of results from DNS of bubbly flows with a two-fluid model for two-dimensional laminar flows. Int. J. Multiph. Flow 31, 1036–1048.

Colin, C., Riou, X., Fabre, J., 2008. Bubble coalescence in gas–liquid flow at microgravity conditions. Microgravity Sci. Technol. 20, 243–246. doi:10.1007/s12217-008-9031-6.

Colin, C., Fabre, J., Dukler, A.E., 1991. Gas–liquid flow at microgravity conditions – I: dispersed bubble and slug flow. Int. J. Multiph. Flow 17, 533–544.

Colin, C., Fabre, J., McQuillen, J., 1996. Bubble and slug flow at microgravity conditions: state of knowledge and open questions. Chem. Eng. Commun. 141–142, 155–173.

Grah, A., Haake, D., Rosendahl, U., Klatte, J., Dreyer, M.E., 2008. Stability limits of unsteady open capillary channel flow. J. Fluid Mech. 600, 271–289.

Haake, D., Rosendahl, U., Ohlhoff, A., Dreyer, M.E., 2006. Flow rate limitation in open capillary channel flows. Ann. N. Y. Acad. Sci. 1077, 443–458.

Kamp, A., Chesters, A.K., Colin, C., Fabre, J., 2001. Bubble coalescence in turbulent flows: a mechanistic model for turbulence induced coalescence applied to bubbly pipe flows under microgravity conditions. Int. J. Multiph. Flow 27, 1363–1396.

Kashinsky, O.N., Timkin, L.S., Cartellier, A., 1993. Experimental study of a laminar bubbly flows invertical pipe. Exp. Fluids 14, 308–314.

Legendre, D., Colin, C., Fabre, J., Magnaudet, J., 1999. Influence of gravity upon the bubble distribution in a turbulent pipe flow: comparison between numerical simulations and experimental data. J. de Chim. Phys. 96, 951–957.

Lu, J., Biswas, S., Tryggvason, G., 2006. A DNS study of laminar bubbly flows in a vertical channel, Int. Int. J. Multiph. Flow 32, 643–660.

Rivière, N., Cartellier, A., 1999. Wall shear stress and void fraction in Poiseuille bubbly flows: part 1 simple analytic predictions. Eur. J. Mech. – B/Fluids 18, 823–846.

Rosendahl, U., Dreyer, M.E., 2007. Design and performance of an experiment for the investigation of open capillary channel flows. Exp. Fluids 42, 683–696.

Rosendahl, U., Ohlhoff, A., Dreyer, M.E., Rath, H.J., 2001. Critical velocity in open capillary channel flows. AIAA 2001, 5021.

Rosendahl, U., Ohlhoff, A., Dreyer, M.E., 2004. Choked flows in open capillary channels: theory, experiment and computations. J. Fluid Mech. 518, 187–214.

Salim, A., Colin, C. Dreyer, M., 2009, Experimental investigation of a bubbly flow in an open capillary channel in microgravity conditions. Microgravity Sci. Technol. doi:10.1007/s12217-009-9115-y.

Song, Q., Luo, R., Yang, X.Y., Wang, Z., 2001. Phase distributions for upward laminar dilute bubbly flows with non-uniform bubble sizes in a vertical pipe. Int. J. Multiph. Flow 27, 379–390.

Takamasa, T., Iguch, T., Hazuku, T., Hibiki, T., Ishii, M., 2003. Interfacial area transport of bubbly flow under microgravity environment. Int. J. Multiph. Flow 29, 291–304.

Tomiyama, A., Tamai, H., Zun, I., Hosokawa, S., 2002. Transverse migration of single bubbles in simple shear flows. Chem. Eng. Sci. 57, 1849–1858.

White, F., 1986. Fluid Mechanics. McGraw-Hill, New York.

Zuber, N., Findlay, J.A., 1965. Average volumetric concentration in two-phase flow systems. J. Heat Transfer 87, 453–468.